
Article:
Chechik, L. orcid.org/0000-0002-7626-2694 and Todd, I. (2023) Inconel 718 two ways: powder bed fusion vs. directed energy deposition. Additive Manufacturing Letters, 6. 100145. ISSN 2772-3690

https://doi.org/10.1016/j.addlet.2023.100145

Additive Manufacturing Letters 6 (2023) 100145

Contents lists available at ScienceDirect

Additive Manufacturing Letters

journal homepage: www.elsevier.com/locate/addlet

Short Communication

Inconel 718 two ways: Powder bed fusion vs. directed energy deposition

Lova Chechik*, Iain Todd

Department of Materials Science and Engineering, The University of Sheffield, Mappin Street. S1 3JD, United Kingdom

ARTICLE INFO

Keywords:
Additive manufacturing
Laser deposition
Powder bed fusion
Directed energy deposition
Nickel superalloys

ABSTRACT

Additive manufacturing (AM) research has grown massively in the last few decades, with applications ranging from the medical sector to automotive. AM of nickel superalloys is of great interest for the aerospace sector due to their mechanical performance at increased temperatures. Components were manufactured using the two most common metallic AM processes, laser powder bed fusion (L-PBF) and laser directed energy deposition (L-DED). Microstructural and mechanical properties were compared and contrasted between the two processes, showing that despite the processes fundamentally being based on the same physical phenomena, the difference in scale between the processes stops them from being directly comparable. As such, alloy design and processing window development must be performed with a specific application and process in mind.

Introduction

Additive manufacturing (AM) of nickel superalloys is of significant industrial interest, notably in the aerospace sector, as a result of their superior mechanical properties at elevated temperatures [1,2]. Many of the highest temperature-capable alloys experience cracking during AM, mainly due to hot tearing and liquation cracking [3,4]. As such, widespread efforts exist to alter existing alloys and design new ones, which exhibit the mechanical properties required whilst being printable without experience cracking and other defects [3,5–9]. Many of these develop an alloy to be “more printable”, but do not design for a specific manufacturing process [5,8,9].

Two of the most common metal AM processes are laser powder bed fusion (L-PBF) and laser directed energy deposition (L-DED). L-PBF is generally used for rapid prototyping and creating lightweight complex geometries, such as the GE LEAP fuel nozzle [10], whilst L-DED is more suited to larger components and repair applications [1]. It has been previously reported that the printability of certain alloys may vary on the chosen AM process [7,11]. The productivity of L-DED is reported to be 5x higher than L-PBF, although lacking the geometric precision of L-PBF [12].

Despite the processes both being fundamentally based on laser welding, the laser is typically an order of magnitude larger in L-DED, the laser power 2–5x larger and the velocity 1–2 orders of magnitude smaller [1,2]. This results in a vastly different thermal conditions within the two processes, where a normalised energy density (NED, E^*) can be defined as $E^* = \frac{P^*}{v^* l^* h^*}$, where P is the laser power, v is the laser velocity, l is the layer thickness, h is the hatch spacing and * denotes a normalised value [13]. This can be calculated as $E^* = \frac{AP}{2vlh}\frac{\alpha}{\kappa(T_m - T_0)}$, where A is the absorptivity, α is the thermal diffusivity, κ is the thermal conductivity, T_m is the melting point (solidus) and T_0 is the initial temperature. Alternatively, the beam radius (r_b) is occasionally used in place of hatch spacing [13,14], resulting in $E_r^* = \frac{P^*}{v^* l^* r_b^*} = \frac{AP}{2vlr_b}\frac{\alpha}{0.67\kappa(T_m - T_0)}$, which will be called NED_r.

It has been previously reported that energy density is an imperfect measure [14,15] and a normalised enthalpy (NE, $\frac{\Delta H}{h_s}$) is intermittently utilised, despite not including factors such as the hatch spacing [16,17]; normalised enthalpy, $\frac{\Delta H}{h_s} = \frac{AP}{\kappa T_m}\sqrt{\frac{\alpha}{\pi v(2r_b)^3}}$. Overall, when comparing the effect of the key processing parameters (nominally power and velocity), these equations simplify to $E^* \propto E_r^* \propto \frac{P}{v}$ and $\frac{\Delta H}{h_s} \propto \frac{P}{\sqrt{v}}$, which have different assumptions about the sensitivity of the process to laser velocity. Both NED and NE are measures of how much energy is required to melt a certain amount of material and so should be reflected in the thermal signature of the process; these values are often experimentally correlated with measures such as the density [13,15] or the shape of single weld tracks (unstable weld track, conduction mode, keyhole mode) [14]. The assumption is that if a similar amount of energy is input into the material (no matter which process parameter combination is used), the output (density, structure) should be similar.

Inconel 718 is a precipitation strengthened nickel superalloy, relying on ordered precipitates, γ' and γ'', for its enhanced mechanical properties [18,19]. Additionally, Laves phases are often present, which are deleterious to mechanical properties [12,20]. Laves phases are reported to be found in both L-PBF [18–21] and L-DED [12,22] samples, with a greater particle size in the latter [12]. The presence of γ' and γ'' precipitates in as-built AM components is an unresolved matter. Precipitates are confirmed to occur in heat treated samples, but in the as-built L-PBF

* Corresponding author.
E-mail address: lchechik@live.co.uk (L. Chechik).

https://doi.org/10.1016/j.addlet.2023.100145
Received 20 December 2022; Received in revised form 30 April 2023; Accepted 7 May 2023

Table 1
Summary of processing parameters used for both L-PBF and L-DED samples; H and L representing high and low energy densities respectively, materials/thermal paramters for NED and NE calculations taken from [23].

Process	Power (W)	Velocity (mm/s)	Hatch Spacing (μm)	Z Step (μm)	Mass flow (g/min)	NED E^*	NED$_r$ E_r^*	NE: $\frac{\Delta H}{h_s}$	Name
L-PBF (Aconity)	95	1000	45	30	N/A	3.8	7.2	4.7	–
	130					5.2	9.9	6.5	PBF_H
	95	1500				2.5	4.8	3.9	PBF_L
	130					3.4	6.6	5.3	–
L-DED (BeAM)	223	33.3	400	200	5.5–6.5	4.5	7.7	1.9	–
	359					7.2	12.3	3.1	DED_H
	223	50				3.0	5.1	1.6	DED_L
	359					4.8	8.2	2.5	–

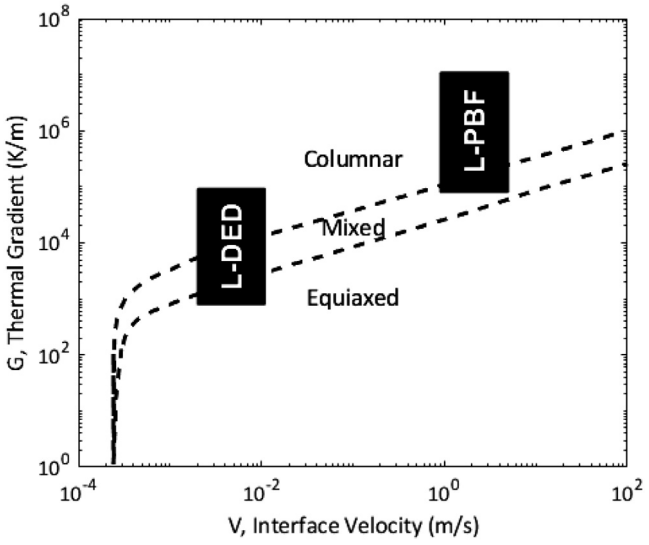

Fig. 1. G vs V plot showing the approximate ranges covered by both L-PBF and L-DED for Inconel 718. Adapted from Dehoff et al. [26].

condition these precipitates are not found [12,19]. In L-DED, it seems that in larger components (where more *in-situ* heat treatment occurs), some γ'/γ'' nano-precipitates can be observed [23,24], but this is very process/parameter dependant [12,25].

Fig. 1 shows the expected microstructural transition from columnar to equiaxed grains with thermal gradient (G) and solidification velocity (V) for Inconel 718 [26], showing that L-PBF is expected to result in a more columnar structure. The laser diameter in L-PBF is typically an order of magnitude smaller than that in L-DED, resulting in a smaller melt pool, which is expected to result in a higher cooling rate [27,28]. It is reported that the cooling rate ($\dot{T}$) in L-PBF is 10^3x greater than in L-DED [2,29], this corresponds to the values which can be calculated from Fig. 1 using $\dot{T} = GV$.

Further, the increased scanning velocities in L-PBF result in increased solidification velocities as well as the higher thermal gradients [29]. The scale of the microstructure is commonly related to the thermal gradient [30–32], with high thermal gradients decreasing the scale of the microstructure (primary dendrite arm spacing, PDAS). The mechanical properties of a material can be correlated to the size of the microstructure, with a finer microstructure resulting in a higher yield strength as summarised by the Hall-Petch equation [33,34]. Additionally, increasing the thermal gradient can lead to a change in solidification structure from dendritic solidification to cellular solidification [35].

Several comparisons between L-PBF and L-DED exist, mainly discussing hybrid manufacturing methods and concluding that the scale of microstructure is smaller in L-PBF than in L-DED [12,29,36–38]. It has been shown that in Inconel 625 (a similar FCC nickel superalloy), L-PBF exhibits increased hardness [37], which was attributed to the finer microstructure when compared to L-DED [38]. Martin et al. reported that the texture is weaker in L-PBF than in L-DED. Godec et al. published the only known work reporting metallographic differences in Inconel 718 between L-PBF and L-DED [12], the focus of which was the mechanical properties in the joint between components manufactured with the different methods. The grain structure was found to be more columnar and with a greater texture in L-PBF, dislocations were found to form a regular cellular substructure. In contrast, larger grains were found in L-DED, with a dendritic structure and a less ordered dislocation structure due to less misorientation. In both structures, Laves phases were found, with some Al_2O_3 oxides; again, at a larger scale in L-DED [12].

In this study, we examine the processing windows of Inconel 718 using both L-PBF and L-DED, quantifying the range of achievable microstructures. The effectiveness of energy density measures is assessed and the feasibility of knowledge transfer between the two processes is explored. By analysing the variety of solidification and grain structures possible in the two processes, the observed hardness trends are explained – highlighting the key differences between the resultant microstructures.

Method and materials

Samples were made in Inconel 718 using both the Aconity3D Mini (L-PBF) and the BeAM Magic 2.0 (L-DED). The L-DED samples were made using a bidirectional hatch strategy, 3 hatches wide (20 mm long, 9.8 mm tall). The L-PBF samples were printed to dimensionally replicate these, with hatching along the length of the wall and dimensions of 2.95×20×9.8 mm (width, length, height respectively). The processing parameters for both processes are summarised in Table 1, these were chosen to capture a wide processing window whilst retaining high density and satisfactory surface finish (established using literature parameters as a starting point).

The range of processing parameters was extended to test the variety of possible grain structures whilst retaining build quality. For L-PBF, there was a 1.7x spread in $\frac{\Delta H}{h_s}$ values (2.1x spread in E^*/E_r^* values); for L-DED, there was a 2.0x spread in $\frac{\Delta H}{h_s}$ values (2.4x spread in E^*/E_r^*).

For each printed sample, thermal monitoring was recorded. On the Aconity3D Mini, a spot pyrometer (Kleiber KG 740 LO) was used, which absorbs photons of a set wavelength range (1580–1800 nm) and the output signal (mV) is proportional to the intensity of the light hitting the sensor. Any output signal below 850 mV was removed to remove ambient noise. A Basler acA1440–73 g coaxial camera was used on the BeAM Magic 2.0 to record the meltpool (75 fps, 4000 μs exposure time, 500×500 px area). A thermal intensity was calculated, which is a sum of all the pixels in the image [23]; effectively, this is what a spot pyrometer does; all thermal intensity values below 0.2×10^7 were removed. As such, the monitoring methods between the two processes are comparable. Their sensitivities may be different, but the measurement methodology is the same.

The extreme sets of parameters were defined as PBF_L/DED_L for low heat input and PBF_H/DED_H for high heat input and were further analyzed. Hardness maps (Durascan 70 Vickers indentor, 1 kg load) were

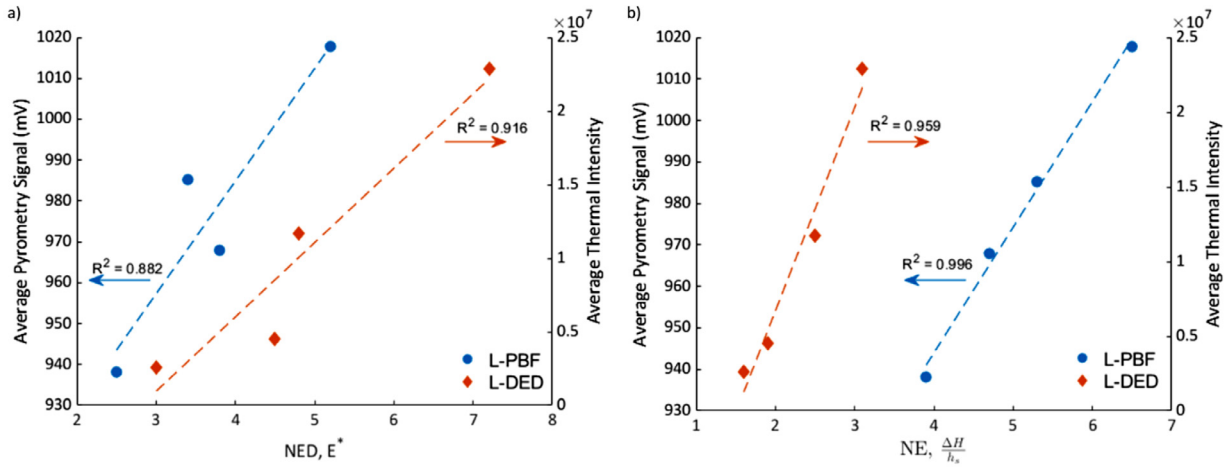

Fig. 2. Correlation of the average pyrometry signal (L-PBF) and thermal intensity (L-DED) with a) E^* and b) $\frac{\Delta H}{h_s}$, for the second half of the build. R^2 values included.

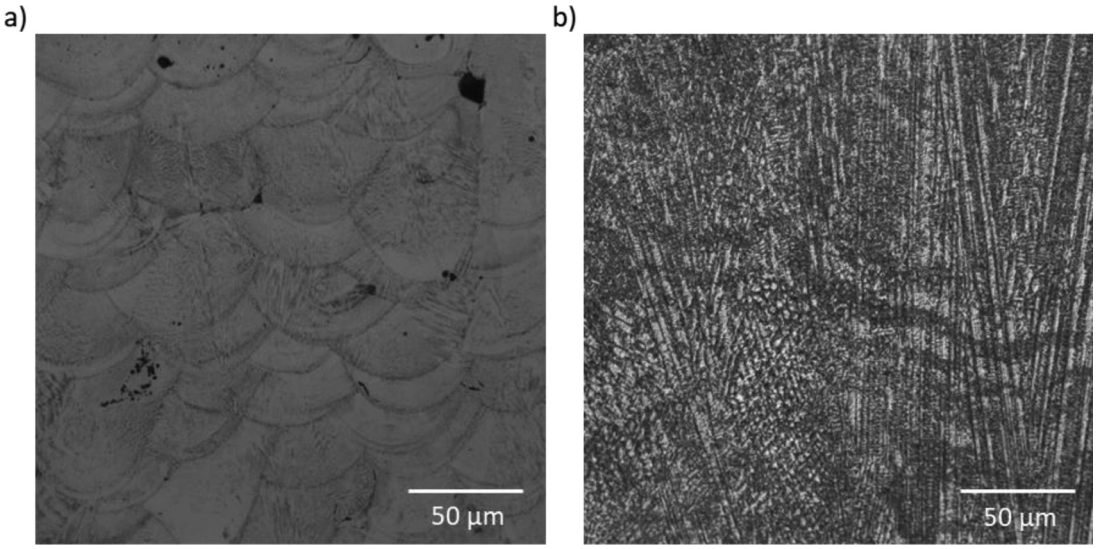

Fig. 3. High resolution optical micrographs of etched samples, with the microstructure visible; (a) L-PBF; (b) L-DED.

taken of the YZ sections with a 0.5 mm step size in both axes. These allowed for both a measure of hardness variation within each component and a comparison of the average hardness values. 2 sample t-tests were performed (α=0.05) to determine whether or not the average hardness values were significantly different from one another.

EBSD analysis was performed using a Jeol 7900F with an Oxford Instruments Symmetry EBSD detector and a 13 mm work offset, with an accelerating voltage of 20 kV. The step size for each scan was between 1 and 1.66 µm. For each sample, a region of 750×5000 µm (Y, Z respectively) was extracted and was further analyzed for grain area, aspect ratio, anisotropy factor (0 for <100> and 0.33 for <111>) [28,39] and maximum mud. Additionally, the grain average misorientation (GAM, which is an average of the kernel average misorientation [40]) was calculated to get an estimate of dislocation density [41,42]. The grain areas in the samples vary greatly, with some directional grains and some equiaxed grains, as a result, each of the measures was weighted by the grain area rather than taking a simple average with equal weightings.

PBF_L and PBF_H samples were polished and etched with Glyceregia; DED_L and DED_H samples were polished and etched with Kallings Reagent #2. Melt pool dimensions were measured from the top row of melt pools as these were not remelted by subsequent layers; for L-PBF several melt pools were measured and so could be averaged; for L-DED, since only 3 hatches were printed, the dimensions of the central melt pool were taken. PDAS were manually measured in a variety of locations within each sample and averaged.

Results and discussion

Thermal monitoring

To get an average thermal signature for each component, an average signal was measured per layer and these layer signals were averaged for the top half of the build (to remove baseplate effects). To compare the accuracy of NED ($E^* \propto E_r^* \propto \frac{P}{v}$ within a process, with constant material and hatching, so E^* will be used going forward) and NE ($\frac{\Delta H}{h_s} \propto \frac{P}{\sqrt{v}}$), both of these were plotted in Fig. 2 against the average pyrometry signal for L-PBF and average thermal intensity for L-DED. Since both <y $E^*$and $\frac{\Delta H}{h_s}$ were developed as a measure of energy required to melt a volume of material, they would be expected to correlate with the thermal signatures of the processes. Unfortunately, due to the different optical setups between L-PBF and L-DED, different monitoring techniques were used and so the thermal signatures cannot be directly compared between the processes.

Normally, these parameters are used for process optimization using single weld tracks; however, here, thermal data from multiple hatches

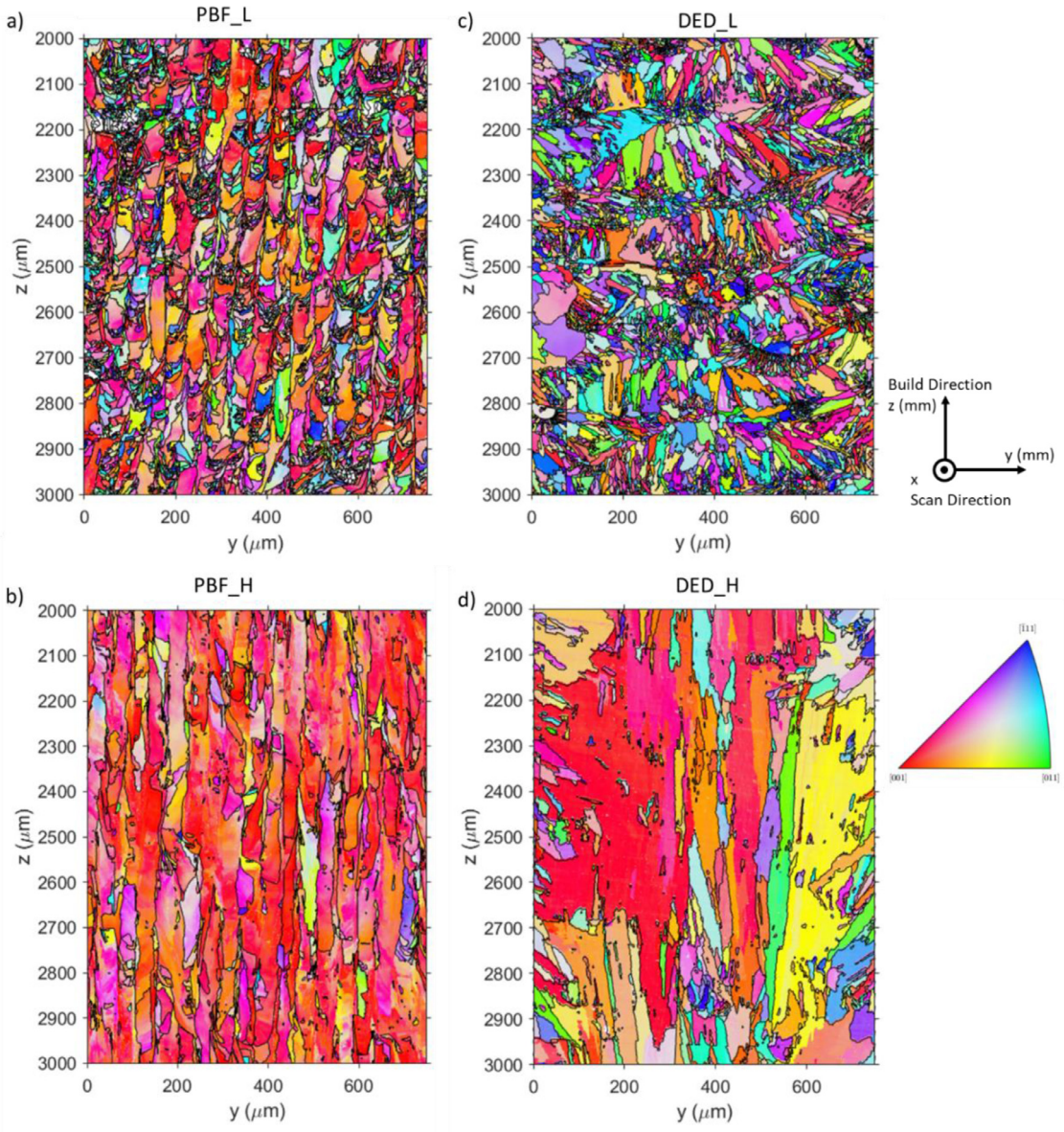

Fig. 4. EBSD orientation maps (IPFX) of the YZ section. (a) PBF_L; (b) PBF_H; (c) DED_L; (d) DED_H.

and layers was used. For both L-PBF and L-DED, both $E^*$and $\frac{\Delta H}{h_s}$ show strong positive correlations, with the latter (NE) being greater for both processes. This suggests that when using these parameters for process optimization, NE is more representative of AM (both L-PBF and L-DED) than NED.

Microstructural analysis

The melt pools in L-DED are both wider and deeper than in L-PBF and the melt pool dimensions in both processes follow the expected trends, being larger in the high heat input samples (Table 2). The large increase in melt pool depth in the PBF_H sample is due to keyholing.

In terms of the microstructure, it is widely disputed whether cells or dendrites are seen in AM. In L-DED micrographs (Fig. 3b), dendritic perturbations can be seen, so these will be referred to as cellular dendrites; in L-PBF, no perturbations can be seen, so these will be referred to as cells. The spacing of both of these will be termed PDAS (λ_1) and are summarised in Table 2. Increasing the thermal gradient leads to a transition from columnar dendritic structures to cellular structures [32]; this is a complex relationship, as cellular structures are possible at both low and high thermal gradients [35,43]. The higher thermal gradients in L-PBF (Fig. 1) explain why the microstructure in these samples is of a more cellular nature than the L-DED process [32].

Table 2
Comparison of melt pool dimensions and PDAS between L-PBF and L-DED. Standard deviations in brackets, for L-DED samples, melt pool dimension errors are the measurement resolution.

Sample	Melt Pool Width (μm)	Melt Pool Depth (μm)	λ_1 (μm)
PBF_L	73.1 (14.0)	48.1 (12.5)	1.1 (0.1)
PBF_H	78.7 (7.0)	112.1 (14.0)	1.0 (0.2)
DED_L	780 (1)	274 (1)	1.8 (0.5)
DED_H	973 (1)	406 (1)	3.0 (0.5)

There are many calculations for the PDAS, the general relation is $\lambda_1 \propto G^{-\frac{1}{2}}$ [30,31]. This may not hold for all temperatures, but seems applicable in Inconel 718 under similar conditions [44–46]. Using the measured PDAS, a cooling rate can be calculated using two different equations by Trivedi and Hunt [30,31], as summarised for Inconel 718

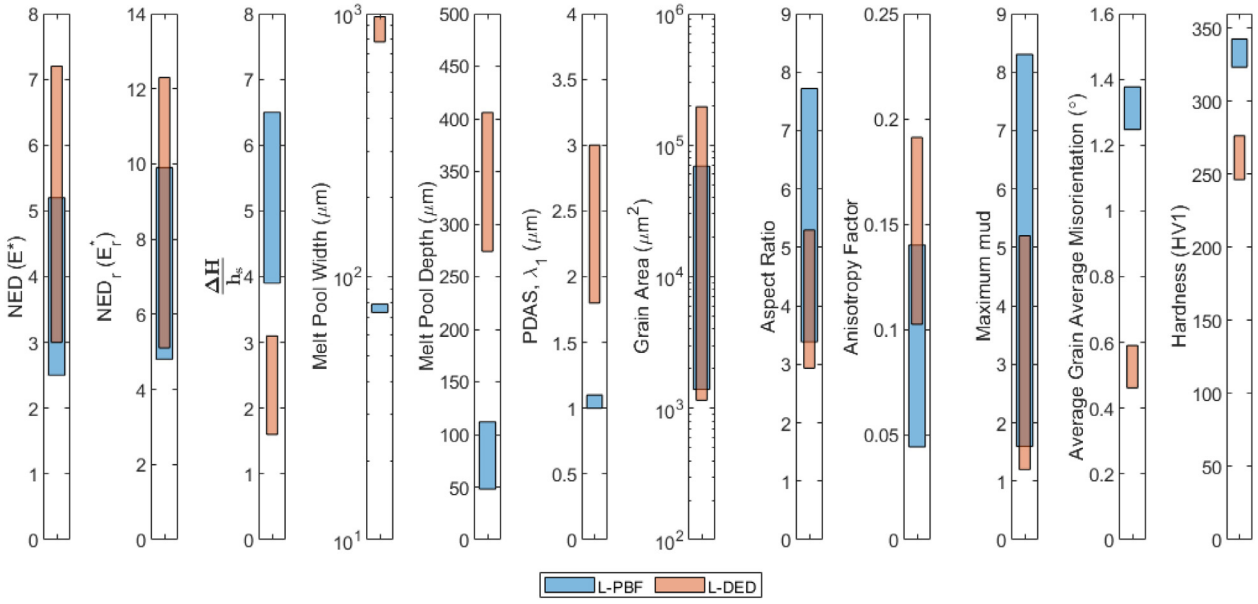

Fig. 5. Comparison of the ranges of characteristic properties between L-PBF and L-DED; including energy densities, melt pool dimensions, grain structure and hardness.

by Raghavan et al. [46]. Using both equations, a range of cooling rates of $9 \times 10^4 - 7 \times 10^5$ K/s are calculated for L-DED, with a range of $5{\times}10^6 - 1{\times}10^7$ K/s for L-PBF. These are higher than those predicted in literature [2], but given the simple nature of the calculations, they are as close to reported values as could be reasonably expected.

Despite similar increases in energy density, the PDAS change in L-PBF is negligible when compared to the PDAS change in L-DED. This is a result the greater cooling rates in L-PBF – at high cooling rates, even a small change in PDAS would require a large change in cooling rate. In contrast, because of the lower cooling rates in L-DED, the calculated change in cooling rate is enough to cause a 1.7x increase in PDAS between DED_L and DED_H.

Grain structure

EBSD grain orientation maps are shown in Fig. 4; step sizes in the range 1.0–1.66 μm were used for different EBSD scans which is significantly smaller than the typical grain size, so this variation in step size is not expected to have any effect on the final results. Fig. 4a and b are L-PBF samples and both appear to consist predominantly of <100> orientated grains leading to a lower anisotropy factor than in L-DED (Fig. 5), which strayed from the <100> orientation (Fig. 4c and d). The range of anisotropy factor values is however larger for L-PBF so there is a larger possible spread in grain orientations. The aspect ratios of grains from both processes are relatively high, with L-PBF having a much larger maximum aspect ratio as a result of the columnar structure seen in Fig. 4b. This was predicted by the location of the L-PBF process on the G-V plot (Fig. 1), with L-PBF being centred in the columnar region, whilst L-DED being centred in the mixed region. For both processes, the low heat input samples had weak texture and so low maximum mud values; the PBF_H sample had by far the strongest texture (<100> orientation) and had the highest maximum mud.

The grain average misorientation (GAM) for each grain is plotted in Fig. 6; the L-PBF samples both have higher GAM than the L-DED samples. This is interesting, as within each sample, the larger grains experience higher GAM values, so one might expect the larger grains in L-DED to have higher GAM values than in L-PBF. Since the thermal gradients in L-PBF are much higher than in L-DED, the structure is cellular rather than cellular dendritic [19,47]. Each grain contains many cells, which are misorientated with respect to one another, and importantly, the cell walls are made up of dislocations [18,19]. Given that L-PBF contains cells (unlike L-DED), this explains the higher GAM values measured when compared to L-DED.

Table 3
Comparison of hardness values between L-PBF and L-DED.

Sample	Average Hardness (HV)	Standard Error
PBF_L	323.4	3.1
PBF_H	342.6	0.9
DED_L	276.4	3.6
DED_H	246.4	3.0

Hardness analysis

The average hardness values of the samples are shown in Table 3; the hardness of L-PBF samples is much greater than that of L-DED samples (Fig. 5). Pairwise 2 sample t-tests were performed and confirmed that the hardness of each sample is significantly different from every other sample (using α=0.05). In L-PBF, the higher energy input sample was found to be hardest, whilst in L-DED, the lower energy input sample was found to be hardest. Since the components being printed here are narrow and with the same experimental setup as [23], it is assumed that none of the samples exhibit significant amounts of γ'/γ'' precipitation in the as-built state. As such it is concluded that the precipitates within the printed components are not responsible for the observed changes in mechanical properties.

The Hall-Petch effect can be used to correlate yield strength to the grain size using $\sigma_y \propto d_g^{-1/2}$ where d_g is the grain diameter [33,34]. Hardness is proportional to yield strength [48,49], so $HV \propto d_g^{-1/2}$. When the grain diameter is small, then even a small change in grain diameter is sufficient to affect the hardness as hardness is more sensitive to grain size changes in smaller grains. As such, we would expect changes in grain size in L-PBF to have a greater effect on the hardness values than changes in L-DED grain size. Despite this, the range of L-DED grain size is so much greater than in L-PBF that it is estimated that the L-DED hardness increase due to grain size is 35% greater than that in L-PBF.

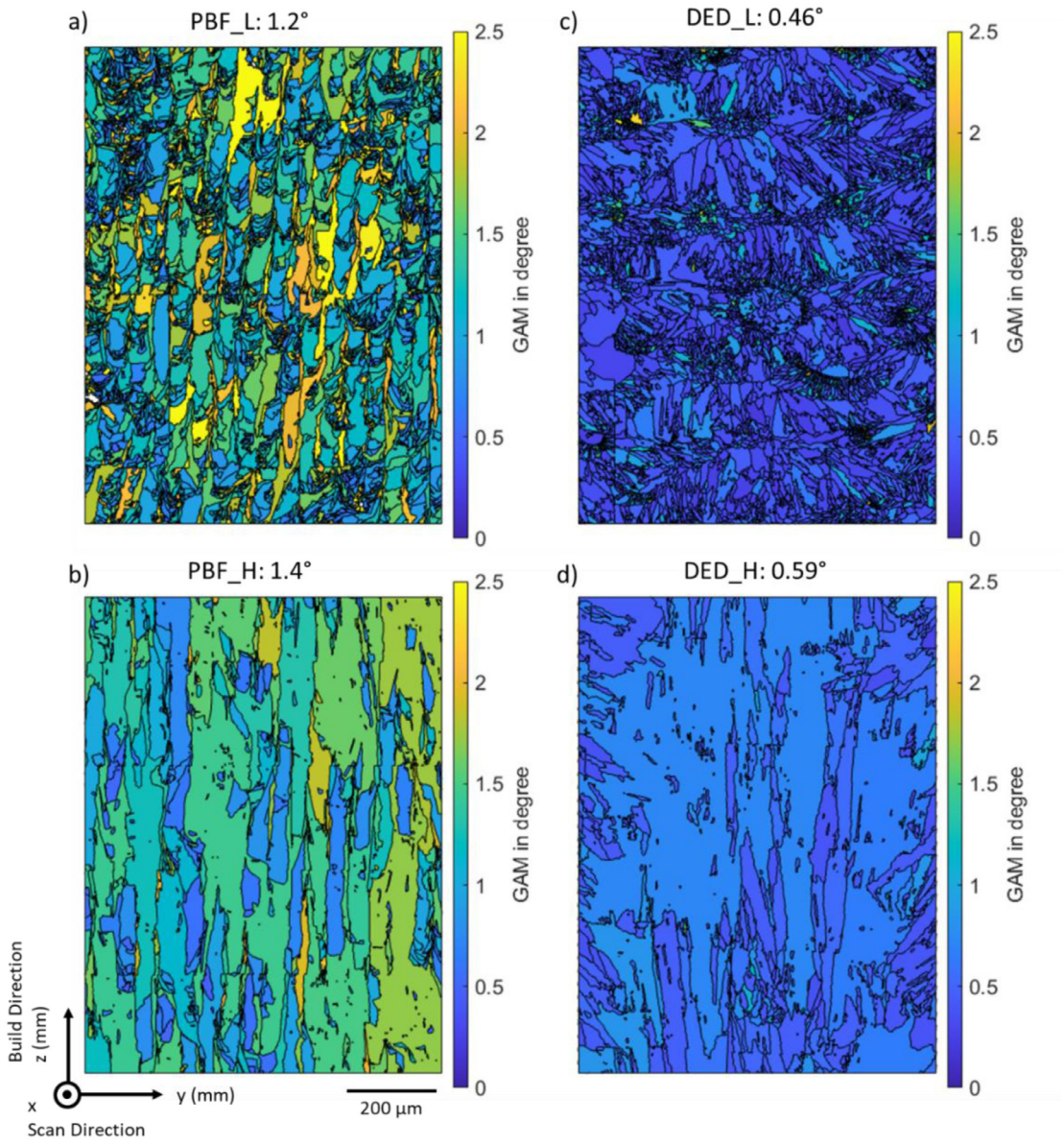

Fig. 6. Maps of the grain average misorientation (GAM) in the YZ sections. (a) PBF_L; (b) PBF_H; DED_L; DED_H. Area-weighted average GAM values included in labels.

Dislocation density, $\rho_d \propto GAM$, so GAM can be used as a proxy for dislocation density [41,42,50]. A grain boundary is a discontinuity in lattice orientation so grain boundaries are essentially areas of high dislocation density. Large grains typically experience greater misorientation within them (seen in Fig. 6b), lattice imperfections such as dislocations must be present to accommodate this misorientation. Conversely, in small grains, only small regions of "perfect" lattice are needed, so small grains are much more likely to have low GAM values. This explains the trends seen in L-DED, with small grains having lower GAM values.

This can be formalised by calculating the energy stored due to dislocations, $E_{dis} \propto \frac{\theta \rho_d}{D_{sub}}$, where θ is the misorientation angle (proportional to GAM) and D_{sub} is the subgrain diameter [51]. In the L-PBF samples, D_{sub} is the cell size, so $E_{dislocations} \propto GAM^2$; since PBF_H has a higher GAM than PBF_L, it is expected to store 34% more energy due to dislocations than PBF_L. PBF_H contains larger grains, which allow for a higher misorientation and a greater stored energy (which is a higher strain). For the L-DED samples, the change in PDAS mean that the stored energy remains basically unchanged between the high and low heat input samples which is surprising, as large grains seem to contain more misorientation (Fig. 6d).

The GAM for the PBF_H sample is 11% higher than for the PBF_L sample, this suggests that the PBF_H sample contains a significantly higher dislocation density than the PBF_L sample. The principal behind work hardening is that as dislocation density increases, the dislocations repel one another, so the material is harder to deform [52]. The relationship $\sigma_y \propto \sqrt{\rho_d}$ has been widely reported [53,54], HV $\approx \sigma_y/3$ [48,49], so $HV \propto \sqrt{\rho_d}$. Zhang et al. report a hardness increase of 28 HV in L-PBF [54], so it is concluded that the hardness increase measured in the L-PBF samples (19 HV) could be explained by the change in the measured dislocation density.

PBF_L contains smaller grains than PBF_H which would be expected to increase the hardness, but also has a lower dislocation density, which would decrease the hardness. It is not obvious which of these phenomena would dominate, but the increased dislocation density in PBF_H could explain the higher hardness measured. In L-DED, due to the lack of cellular structure, the grain boundaries are the main obstacles to dislocation movement and so the Hall-Petch effect explains the trend in

hardness observed. Overall, the L-PBF samples have both smaller grains and higher GAM values than the L-DED samples, which explains why the hardness values in the L-PBF samples are significantly higher than in the L-DED samples.

Conclusions

The resultant microstructure and mechanical properties of a component are dependant on a combination of complex factors including (most significant in bold):

- Laser power
- Laser beam size
- Laser velocity
- Powder size/composition
- Component geometry and scan strategy
- Heat flow mechanisms

Normalised energy densities, NED, are often used for establishing processing parameters which result in high density components. It is shown that for real AM processes, NE is a better measure of the thermal response of the process than NED (Fig. 2). The absolute values of both NED and NE are of the same order of magnitude in both processes (Fig. 5), which is surprising given that the size of the laser sources differ by an order of magnitude.

Despite the NE and NED being similar between the two processes, the melt pool sizes in L-DED were found to be 4–12x larger than in L-PBF, as a direct result of the laser beam diameter. A combination of increased cooling rate (due to increased thermal conduction away from the smaller melt pool) and increased solidification rate (related to the scanning velocity) in L-PBF lead to a greater thermal gradient than in L-DED (Fig. 1).

In L-DED, the grain size is shown to be the key factor affecting to the hardness, with the smaller grains in DED_L (higher thermal gradient) resulting in an increased hardness (following the Hall-Petch relation). In L-PBF, however, the dislocations found due to the cellular structure are the dominant factor affecting hardness. PBF_H is found to have a higher GAM and so a higher dislocation density, resulting in increased hardness despite the increased grain size. Even if an AM component is heat treated, the final mechanical properties are still dependant on the as-built microstructure [55], so the process must be selected with a specific application in mind.

Table 3 shows that as-built mechanical properties of components made by the two processes are significantly different, with L-PBF samples being at least 17% harder than L-DED samples. This difference relatively small, especially compared to the change in cooling rates, which are ~100x different. Even if grain properties were consistent between the processes, the difference in melt pool size and thermal gradients changes the nature of the microstructure (cells vs dendrites) which in turn alters the dislocation structure. This shows that the properties of an additively manufactured component are strongly affected by the process, with these changes reportedly being retained post heat treatment. For a specific application, the desired properties must be specified and both the process and alloy must be selected specifically to match this. It is insufficient to select an alloy and assume that however it is produced, the final component will meet the required mechanical properties.

Declaration of Competing Interest

The authors declare that they have no known competing financial interests or personal relationships that could have appeared to influence the work reported in this paper.

CRediT authorship contribution statement

Lova Chechik: Conceptualization, Methodology, Investigation, Writing – original draft. **Iain Todd:** Conceptualization, Writing – review & editing, Supervision, Funding acquisition.

Data availability

Data supporting this publication can be freely downloaded from https://zenodo.org/record/7863320 under the terms of the Creative Commons Attribution (CC BY) licence.

Acknowledgments

This work was supported by the EPSRC Rolls-Royce Strategic Partnership Grant, MAPP (grant EP/P006566/1) and EPSRC (grant EP/R512175/1). The provision of supporting information from Rolls-Royce plc. is gratefully acknowledged. We also wish to acknowledge the Henry Royce Institute for Advanced Materials, funded through EPSRC grants EP/R00661X/1, EP/S019367/1, EP/P02470X/1 and EP/P025285/1, for Aconity3D Mini and BeAM Magic 2.0 access at The University of Sheffield and also for FEG JSM-7900F SEM access at Royce@Sheffield. Thanks to Dr. Le Ma for operation of the SEM and collected EBSD data. For the purpose of open access, the author has applied a Creative Commons Attribution (CC BY) licence to any Author Accepted Manuscript version arising.

References

[1] B. Blakey-Milner, P. Gradl, G. Snedden, M. Brooks, J. Pitot, E. Lopez, M. Leary, F. Berto, Metal additive manufacturing in aerospace : a review, Mater. Des. 209 (2021) 110008, doi:10.1016/j.matdes.2021.110008.
[2] T. DebRoy, H.L. Wei, J.S. Zuback, T. Mukherjee, J.W. Elmer, J.O. Milewski, A.M. Beese, A. Wilson-Heid, A. De, W. Zhang, Additive manufacturing of metallic components – Process, structure and properties, Prog. Mater. Sci. 92 (2018) 112–224, doi:10.1016/j.pmatsci.2017.10.001.
[3] J.F.S. Markanday, Applications of alloy design to cracking resistance of additively manufactured Ni-based alloys, Mater. Sci. Technol. (2022), doi:10.1080/02670836.2022.2068759.
[4] L.N. Carter, M.M. Attallah, R.C. Reed, Laser powder bed fabrication of nickel-base superalloys : influence of parameters ; characterisation, quantification and mitigation of cracking, Superalloys 2012 (2012) 577–586, doi:10.1002/9781118516430.ch64.
[5] Y.T. Tang, C. Panwisawas, J.N. Ghoussoub, Y. Gong, J.W.G. Clark, A.A.N. Németh, D.G. McCartney, R.C. Reed, Alloys-by-design: application to new superalloys for additive manufacturing, Acta Mater. 202 (2021) 417–436, doi:10.1016/j.actamat.2020.09.023.
[6] B.D. Conduit, T. Illston, S. Baker, D.V. Duggappa, S. Harding, H.J. Stone, G.J. Conduit, Probabilistic neural network identification of an alloy for direct laser deposition, Mater. Des. 168 (2019) 107644, doi:10.1016/j.matdes.2019.107644.
[7] A.T. Clare, R.S. Mishra, M. Merklein, H. Tan, I. Todd, L. Chechik, J. Li, M. Bambach, Alloy design and adaptation for additive manufacture, J. Mater. Process. Technol. (2022) 299, doi:10.1016/j.jmatprotec.2021.117358.
[8] T.M. Pollock, A.J. Clarke, S.S. Babu, Design and tailoring of alloys for additive manufacturing, Metall. Mater. Trans. A Phys. Metall. Mater. Sci. 51 (2020) 6000–6019, doi:10.1007/s11661-020-06009-3.
[9] B. Wahlmann, D. Leidel, M. Markl, C. Körner, Numerical alloy development for additive manufacturing towards reduced cracking susceptibility, 3 (2021).
[10] GEAdditive, New manufacturing milestone: 30,000 additive fuel nozzles, (2018). https://www.ge.com/additive/stories/new-manufacturing-milestone-30000-additive-fuel-nozzles (accessed October 11, 2021).
[11] L. Chechik, K.A. Christofidou, L. Farquhar, M. Tse, G. Baxter, I. Todd, M. Mar, Tools for the assessment of the laser printability of nickel superalloys, Metall. Mater. Trans. A. (2023), doi:10.1007/s11661-023-07029-5.
[12] M. Godec, S. Malej, D. Feizpour, Č. Donik, M. Balažic, D. Klobčar, L. Pambaguian, M. Conradi, A. Kocijan, Hybrid additive manufacturing of Inconel 718 for future space applications, Mater. Charact. 172 (2021) 110842, doi:10.1016/j.matchar.2020.110842.
[13] M. Thomas, G.J. Baxter, I. Todd, Normalised model-based processing diagrams for additive layer manufacture of engineering alloys, Acta Mater. 108 (2016) 26–35, doi:10.1016/j.actamat.2016.02.025.
[14] U. Scipioni Bertoli, A.J. Wolfer, M.J. Matthews, J.P.R. Delplanque, J.M. Schoenung, On the limitations of volumetric energy density as a design parameter for selective laser melting, Mater. Des. 113 (2017) 331–340, doi:10.1016/j.matdes.2016.10.037.
[15] K.G. Prashanth, S. Scudino, T. Maity, J. Das, J. Eckert, Is the energy density a reliable parameter for materials synthesis by selective laser melting? Mater. Res. Lett. 5 (2017) 386–390, doi:10.1080/21663831.2017.1299808.
[16] D.B. Hann, J. Iammi, J. Folkes, A simple methodology for predicting laser-weld properties from material and laser parameters, J. Phys. D Appl. Phys. 44 (2011), doi:10.1088/0022-3727/44/44/445401.
[17] W.E. King, H.D. Barth, V.M. Castillo, G.F. Gallegos, J.W. Gibbs, D.E. Hahn, C. Kamath, A.M. Rubenchik, Observation of keyhole-mode laser melting in laser powder-bed fusion additive manufacturing, J. Mater. Process. Technol. 214 (2014) 2915–2925, doi:10.1016/j.jmatprotec.2014.06.005.
[18] D. Zhang, W. Niu, X. Cao, Z. Liu, Effect of standard heat treatment on the microstructure and mechanical properties of selective laser melting manufactured Inconel 718 superalloy, Mater. Sci. Eng. A 644 (2015) 32–40, doi:10.1016/j.msea.2015.06.021.

[19] M. Pröbstle, S. Neumeier, J. Hopfenmüller, L.P. Freund, T. Niendorf, D. Schwarze, M. Göken, Superior creep strength of a nickel-based superalloy produced by selective laser melting, Mater. Sci. Eng. A 674 (2016) 299–307, doi:10.1016/j.msea.2016.07.061.
[20] X. Wang, X. Gong, K. Chou, Review on powder-bed laser additive manufacturing of Inconel 718 parts, Proc. Inst. Mech. Eng. Part B J. Eng. Manuf. 231 (2017) 1890–1903, doi:10.1177/0954405415619883.
[21] V.A. Popovich, E.V. Borisov, A.A. Popovich, V.S. Sufiiarov, D.V. Masaylo, L. Alzina, Functionally graded Inconel 718 processed by additive manufacturing: crystallographic texture, anisotropy of microstructure and mechanical properties, Mater. Des. 114 (2017) 441–449, doi:10.1016/j.matdes.2016.10.075.
[22] L.L. Parimi, G. Ravi, D. Clark, M.M. Attallah, Microstructural and texture development in direct laser fabricated IN718, Mater. Charact. 89 (2014) 102–111, doi:10.1016/j.matchar.2013.12.012.
[23] L. Chechik, K.A. Christofidou, J.F.S. Markanday, A.D. Goodall, J.R. Miller, G. West, H. Stone, I. Todd, Hardness variation in inconel 718 produced by laser directed energy deposition, Materialia 26 (2022) 101643, doi:10.1016/j.mtla.2022.101643.
[24] Y. Tian, D. McAllister, H. Colijn, M. Mills, D. Farson, M. Nordin, S. Babu, Rationalization of microstructure heterogeneity in Inconel 718 builds made by the direct laser additive manufacturing process, Metall. Mater. Trans. A Phys. Metall. Mater. Sci. 45 (2014) 4470–4483, doi:10.1007/s11661-014-2370-6.
[25] Z. Li, J. Chen, S. Sui, C. Zhong, X. Lu, X. Lin, The microstructure evolution and tensile properties of Inconel 718 fabricated by high-deposition-rate laser directed energy deposition, Addit. Manuf. 31 (2020) 100941, doi:10.1016/j.addma.2019.100941.
[26] R.R. Dehoff, M.M. Kirka, W.J. Sames, H. Bilheux, A.S. Tremsin, L.E. Lowe, S.S. Babu, Site specific control of crystallographic grain orientation through electron beam additive manufacturing, Mater. Sci. Technol. 31 (2015) 931–938, doi:10.1179/1743284714Y.0000000734.
[27] W. Hofmeister, M. Griffith, M. Ensz, J. Smugeresky, Solidification in direct metal deposition by LENS processing, JOM 53 (2001) 30–34, doi:10.1007/s11837-001-0066-z.
[28] L. Chechik, N.A. Boone, L.R. Stanger, P. Honniball, F. Freeman, G. Baxter, J.R. Willmott, I. Todd, Variation of texture anisotropy and hardness with build parameters and wall height in directed-energy-deposited 316L steel, Addit. Manuf. 38 (2021) 101806, doi:10.1016/j.addma.2020.101806.
[29] C. Doñate-Buendia, P. Kürnsteiner, F. Stern, M.B. Wilms, R. Streubel, I.M. Kusoglu, J. Tenkamp, E. Bruder, N. Pirch, S. Barcikowski, K. Durst, J.H. Schleifenbaum, F. Walther, B. Gault, B. Gökce, Microstructure formation and mechanical properties of ODS steels built by laser additive manufacturing of nanoparticle coated iron-chromium powders, Acta Mater. 206 (2021), doi:10.1016/j.actamat.2020.116566.
[30] J.D. Hunt, Cellular and primary dendrite spacings, in: Solidif. Cast. Met., The Metals Society, Sheffield, 1979: p. 3.
[31] R. Trivedi, Interdendritic spacing: Part II. A comparison of theory and experiment, Metall. Trans. A 15 (1984) 977–982, doi:10.1007/BF02644689.
[32] H. Jones, Rapid Solidification of Metals and Alloys, Institution of Metallurgists, London, 1983.
[33] E.O. Hall, The deformation and ageing of mild steel: III Discussion of results, Proc. Phys. Soc. Sect. B 64 (1951) 747–753, doi:10.1088/0370-1301/64/9/303.
[34] J.P. Hirth, J. Lothe, T. Mura, Theory of dislocations (2nd ed.), J. Appl. Mech. 50 (1983), doi:10.1115/1.3167075.
[35] W. Kurz, D.J. Fisher, Fundamentals of Solidification, 4th ed., Trans Tech Publications, 1998.
[36] M. Yan, P. Yu, An overview of densification, microstructure and mechanical property of additively manufactured Ti-6Al-4V — Comparison among selective laser melting, electron beam melting, laser metal deposition and selective laser sintering, and with conventional powder, Sinter. Tech. Mater. (2015). doi:10.5772/59275.
[37] N. Martin, A. Hor, E. Copin, P. Lours, L. Ratsifandrihana, Correlation between microstructure heterogeneity and multi-scale mechanical behavior of hybrid LPBF-DED Inconel 625, J. Mater. Process. Technol. 303 (2022), doi:10.1016/j.jmatprotec.2022.117542.
[38] G. Marchese, G. Basile, E. Bassini, A. Aversa, D. Ugues, P. Fino, S. Biamino, Study of the microstructure and cracking mechanisms of hastelloy X produced by laser powder bed fusion, Materials 11 (2018) 106 (Basel), doi:10.3390/ma11010106.
[39] J.C. Stinville, C. Tromas, P. Villechaise, C. Templier, Anisotropy changes in hardness and indentation modulus induced by plasma nitriding of 316L polycrystalline stainless steel, Scr. Mater. 64 (2011) 37–40, doi:10.1016/j.scriptamat.2010.08.058.
[40] MTEX, Grain Orientation Parameters, (2023). https://mtex-toolbox.github.io/GrainOrientationParameters.html (accessed June 10, 2022).
[41] Z. Zribi, H.H. Ktari, F. Herbst, V. Optasanu, N. Njah, EBSD, XRD and SRS characterization of a casting Al-7wt%Si alloy processed by equal channel angular extrusion: dislocation density evaluation, Mater. Charact. 153 (2019) 190–198, doi:10.1016/j.matchar.2019.04.044.
[42] I. Carneiro, S. Simoes, Recent advances in EBSD characterization of metals, Metals 10 (2020) (Basel), doi:10.3390/met10081097.
[43] W. Kurz, C. Bezençon, M. Gäumann, Columnar to equiaxed transition in solidification processing, Sci. Technol. Adv. Mater. 2 (2001) 185–191, doi:10.1016/S1468-6996(01)00047-X.
[44] S.J. Wolff, Z. Gan, S. Lin, J.L. Bennett, W. Yan, G. Hyatt, K.F. Ehmann, G.J. Wagner, W.K. Liu, J. Cao, Experimentally validated predictions of thermal history and microhardness in laser-deposited Inconel 718 on carbon steel, Addit. Manuf. 27 (2019) 540–551, doi:10.1016/j.addma.2019.03.019.
[45] P. Promoppatum, S.C. Yao, P.C. Pistorius, A.D. Rollett, A comprehensive comparison of the analytical and numerical prediction of the thermal history and solidification microstructure of Inconel 718 products made by laser powder-bed fusion, Engineering 3 (2017) 685–694, doi:10.1016/J.ENG.2017.05.023.
[46] N. Raghavan, S. Simunovic, R. Dehoff, A. Plotkowski, J. Turner, M. Kirka, S. Babu, Localized melt-scan strategy for site specific control of grain size and primary dendrite arm spacing in electron beam additive manufacturing, Acta Mater. 140 (2017) 375–387, doi:10.1016/j.actamat.2017.08.038.
[47] N. Kwabena Adomako, N. Haghdadi, S. Primig, Electron and laser-based additive manufacturing of Ni-based superalloys: a review of heterogeneities in microstructure and mechanical properties, Mater. Des. 223 (2022) 111245, doi:10.1016/j.matdes.2022.111245.
[48] J.R. Cahoon, W.H. Broughton, A.R. Kutzak, The determination of yield strength from hardness measurements, Metall. Trans. 2 (1971) 1979–1983, doi:10.1007/BF02913433.
[49] M.O. Lai, K.B. Lim, On the prediction of tensile properties from hardness tests, J. Mater. Sci. 26 (1991) 2031–2036, doi:10.1007/BF00549163.
[50] P.J. Konijnenberg, S. Zaefferer, D. Raabe, Assessment of geometrically necessary dislocation levels derived by 3D EBSD, Acta Mater. 99 (2015) 402–414, doi:10.1016/j.actamat.2015.06.051.
[51] A. Rollett, F. Humphreys, G.S. Rohrer, M. Hatherly, Recrystallization and related annealing phenomena: second edition, 2004. doi:10.1016/B978-0-08-044164-1.X5000-2.
[52] D. Hull, D.J. Bacon, Introduction to dislocations, 2011. 10.1016/C2009-0-64358-0.
[53] J.E. Bailey, P.B. Hirsch, The dislocation distribution flow stress and stored energy in cold worked crystalline silver, Philos. Mag. 5 (1960), doi:10.1080/14786436008238300.
[54] S. Zhang, X. Lin, L. Wang, X. Yu, Y. Hu, H. Yang, L. Lei, W. Huang, Strengthening mechanisms in selective laser-melted Inconel 718 superalloy, Mater. Sci. Eng. A 812 (2021) 141145, doi:10.1016/j.msea.2021.141145.
[55] S. Sanchez, G. Gaspard, C.J. Hyde, I.A. Ashcroft, G.A. Ravi, A.T. Clare, The creep behaviour of nickel alloy 718 manufactured by laser powder bed fusion, Mater. Des. 204 (2021) 109647, doi:10.1016/j.matdes.2021.109647.